System Identification and Sensor Calibration Methods for Commissioning of Bearingless Machines

Daehoon SUNG*, Takahiro NOGUCHI*, Anirudh UPADHYAYA**, Sang-Guk KANG*** and Eric L. SEVERSON*

* Department of Mechanical Engineering, University of Minnesota
111 Church St SE, Minneapolis, Minnesota, USA
E-mail: sung0058@umn.edu
** Department of Electrical and Computer Engineering, University of Wisconsin-Madison
1415 Engineering Dr, Madison, Wisconsin, USA
*** DEVCOM Army Research Laboratory
Aberdeen Proving Ground, Maryland, USA

Abstract

This paper presents a practical and comprehensive guide for commissioning bearingless machines (BMs). While significant research has been conducted on the commissioning of electric machines (EMs) and magnetic bearings (MBs), relatively little attention has been given to bringing up BMs. Motivated by this gap, the paper presents step-by-step methods for commissioning of BMs. Two major contributions are outlined in the paper. First, static characterization and sensor calibration techniques which are necessary for levitating the machine, are introduced. Second, a system identification (System ID) procedure for each plant is presented. This paper emphasizes practical testing sequences that are immediately applicable to real-world prototyping efforts. By following the procedures provided by the paper, engineers and researchers can efficiently commission BMs while ensuring precise sensor calibration and accurate dynamic modeling.

Keywords : Bearingless machines, commissioning, system identification, frequency response function, sensor calibration, static characterization, levitation control, control signal injection.

1. Introduction

This paper provides a comprehensive guide to the commissioning of bearingless machines (BMs) based on the authors' experience of prototyping and testing numerous types of BMs (ac homopolar, consequent pole, PMSM, and induction). The word "commissioning" in this paper refers to the entire set of procedures required to enable the operation of a bearingless machine (BM), including static characterization, sensor calibration, and system identification (System ID). The paper is motivated by the observation that while there are numerous studies on the commissioning and system identification of electric machines (EMs) and magnetic bearings (MBs), there are nearly no studies on bringing up new BMs. A notable reference on BMs is Petersen et al. (2022), which documents System ID techniques to extract command tracking and disturbance rejection transfer functions of the suspension system; however, it does not provide a procedure to extract the parameters and system properties that are required to commission a new BM. Examples of relevant literature in MBs and EMs include Noshadi et al. (2015), where System ID is used to model MIMO system of active magnetic bearing for robust control, and Beya et al. (2002), which uses frequency response function (FRF) to identify d/q-axis parameters of synchronous machine.

The primary contribution of this paper is to provide step-by-step procedures and testing strategies to commission new BMs. The paper presents practical methods for system characterization and sensor calibration that are to be followed prior to levitation and System ID based on FRFs measured by using control signal injection, which are completed as part of the control tuning process once levitation is achieved.

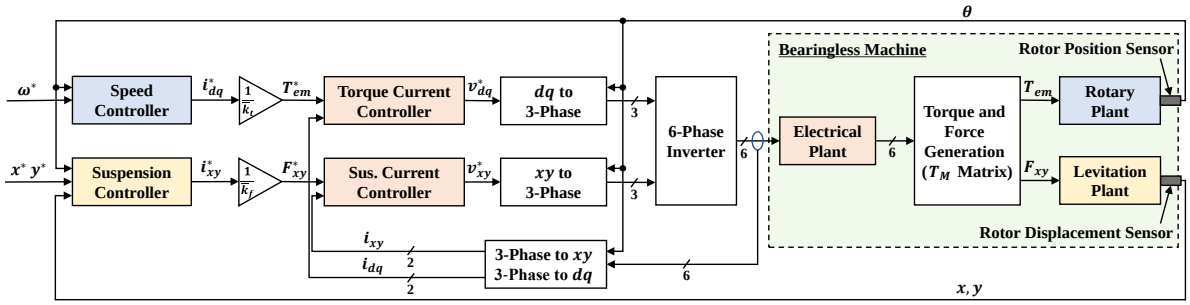

Fig. 1: Control architecture for Bearingless Machine

Table 1: Mathematical expressions of plant models

Electrical Plant	Levitation Plant	Rotary Plant
$\frac{I_{dq}(s)}{V_{dq}(s)} = \frac{1}{L_{dq}s + R_{dq}}$ (1a)	$\frac{x_0(s)}{F_{x_0}(s)} = \frac{1}{ms^2 - k_\delta}$ (2a)	$J\frac{d\omega(t)}{dt} = T_{\text{em}}(t) - b_p\omega(t) - T_\mu \,\text{sign}(\omega)$ (3a)
$\frac{I_{xy}(s)}{V_{xy}(s)} = \frac{1}{L_{xy}s + R_{xy}}$ (1b)	$\frac{\beta(s)}{F_\beta(s)} = \frac{1}{Js^2 - r_\delta^2 k_\delta}$ (2b)	$\frac{\omega(s)}{T_{\text{em}}(s)} = \frac{1}{Js + b_p}$ (3b)

2. Overview of Bearingless Machine Control System

This section introduces the standard control architecture for BMs as shown in Fig. 1. The outer motion controller consists of the Speed Controller and Suspension Controller, while the inner current control loop includes the Torque Current Controller and the Suspension Current Controller. The six-phase currents are transformed into electrical space vectors in different reference frames via the Generalized Clarke Transform to generate torque and suspension force, as explained in Khamitov et al. (2023). The Torque and Force Generation block converts 6-phase currents into torque and force using the T_{m} matrix, which will be discussed in Section 4. This control system requires precise rotor angle and displacement feedback for stable levitation, as well as accurate plant parameters for controller tuning. The transfer functions of the electrical plant are provided in the torque dq Eq. (1a) and the suspension xy Eq. (1b) frame in Table 1 including the plant parameters of inductance (L_{dq}, L_{xy}) and resistance (R_{dq}, R_{xy}). The rotational dynamics of the rotor around the z-axis are described by Eq. (3a), where J is the rotor's moment of inertia, $\omega(t)$ is the angular velocity, $T_{\text{em}}(t)$ is the electromagnetic torque, b_p is the damping coefficient, and T_μ is the friction torque. When the friction torque T_μ is small enough to be neglected, which is typically true in BMs, the rotary motion transfer function can be approximated as Eq. (3b). This paper presents practical methods to determine accurate values for these parameters as observed by the BM drive.

The control system drawing of Fig. 1 corresponds to a single rotor/stator. This paper assumes the control system is extended to have a pair of BMs using centralized control, as discussed in Maslen et al. (2009). Fig. 2 shows a rigid body shaft model about xz-axis under centralized control for a 4 degree-of-freedom (4-DOF) system. x_0 denotes the distance from the z-axis to the center of mass of the rotor, while β is the angle between the z-axis and the shaft. For yz-axis, y_0 and α are defined analogously to x_0 and β. Based on this, the levitation plant models are shown in the translational Eq. (2a) and rotational Eq. (2b) domains, where m is the rotor mass, k_δ is the stiffness coefficient, J is the rotational inertia, and r_δ is the distance between the actuator and the center of mass.

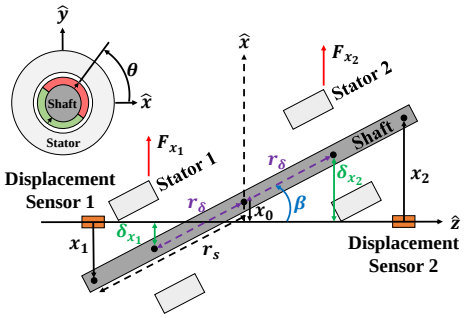

Fig. 2: Rigid body shaft model in xz-axis.

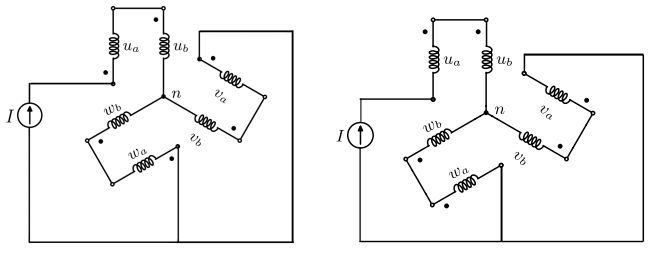

(a) Torque (b) Force

Fig. 3: Winding connection for measuring (a) torque, and (b) force.

There are several types of winding topologies used to create torque and suspension force in BMs, e.g., separated, multiphase, parallel dual purpose no voltage (DPNV), middle-point current injection, and bridge DPNV, as presented in Khamitov et al. (2023). The procedures presented in this paper apply to all of these types. At the early stages of characterization, it is convenient to use a single DC supply instead of a multiphase drive to create shaft torque or force. In separated windings, this is readily accomplished by connecting the supply to either the suspension or torque winding. This can also be accomplished for any combined winding by connecting the winding phases as indicated in Fig. 3. This figure uses DPNV nomenclature (i.e., coil groups u_a, u_b) which are mapped to multiphase winding nomenclature (phase 1, 2, etc) as summarized in Table I of Khamitov et al. (2023).

3. Description of required hardware

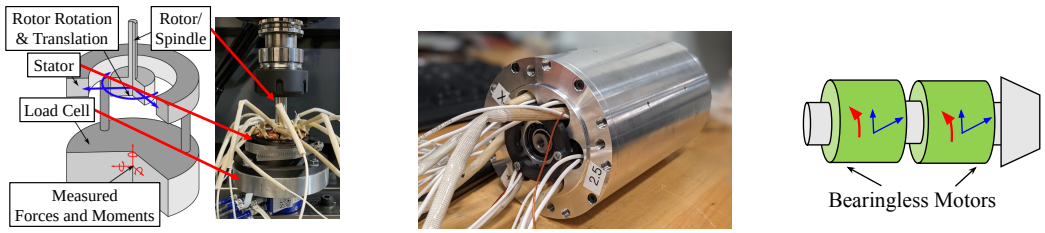

(a) (b) (c)

Fig. 4: (a) Mill setup of bearingless dynamometer, (b) BM prototype, and (c) 4-DOF diagram

This section introduces two test stands that are needed for commissioning BMs: 1) a static test stand with means to measure force/torque and precisely position the rotor, and 2) a bearingless motor with appropriate sensors (encoder, eddy current sensors), backup bearings, and a drive that supports signal injection, variable logging, and a programmable encoder offset angle. For the static test stand, a contactless dynamometer, as shown in Fig. 4 (a), is needed to measure multi-axis forces and moments on the stator. In this example test stand, the rotor is actuated by a spindle of a CNC mill, allowing accurate motion control (x – y movement and rotary angle). A similar configuration with an appropriate load cell is recommended for precise torque and force measurement. For the second test stand, eddy current sensors are assumed for accurate measurement of radial displacement and a precise non-contact rotor angle sensor is essential for the accurate control of BMs. In the authors' example hardware, a rotary magnetic encoder with 1024 pulses per revolution is used to measure the position of the rotor without physical contact. Fig. 4 (b) shows the BM prototype used in this paper, which has a rated power of 15 kW and a rated speed of 160 kRPM. It consists of twin BMs to enable 4-DOF as illustrated in Fig. 4 (c).

4. System characterization measurements

This section proposes procedures to measure the machine's constants using the static test stand described in Section 3. The constants of interest are presented in Table 2 along with governing equations relating these constant to the BM's electrical and mechanical behavior using the notation of Khamitov et al. (2023).

4.1. Displacement stiffness

Displacement stiffness k_δ in BMs refers to the destabilizing radial electromagnetic force $\vec{F}$ generated by the stator in response to rotor displacement $\vec{\delta}$ from the magnetic center. To estimate k_δ, the rotor is rotated fully at different radial positions shown in Fig. 5 (a). To better visualize both the magnitude and angle of the force vector, the force components measured through the load cell are illustrated in polar coordinates as shown in Fig. 5 (b) and (c). At the center of the radial displacement grid, the rotor is at the magnetic center, where the force magnitude is near zero across a full electrical cycle and the angle rotates 360 degree. k_δ is determined by the slope of the linear fit based on the Eq. (4) as shown in Fig. 5 (d). In this case, the resulting stiffness is approximately 6.76 kN/m.

Table 2: Static model equations of stiffness, torque, force, back-EMF, and T_m matrix

Displacement Stiffness	Torque Constant	Force Constant	Back-EMF Constant	$\mathbf{T_m}$ matrix
$\vec{F} = k_\delta \vec{\delta}$ (4)	$\vec{T} = k_\mathrm{t} \vec{i}_\mathrm{t}$ (5)	$\vec{F} = k_\mathrm{f} \vec{i}_\mathrm{s}$ (6)	$v_\mathrm{m} = k_\phi \omega$ (7)	$\mathbf{F}(\theta) = T_\mathrm{m}(\theta)\mathbf{i} + M_\mathrm{c}(\theta)$ (8)

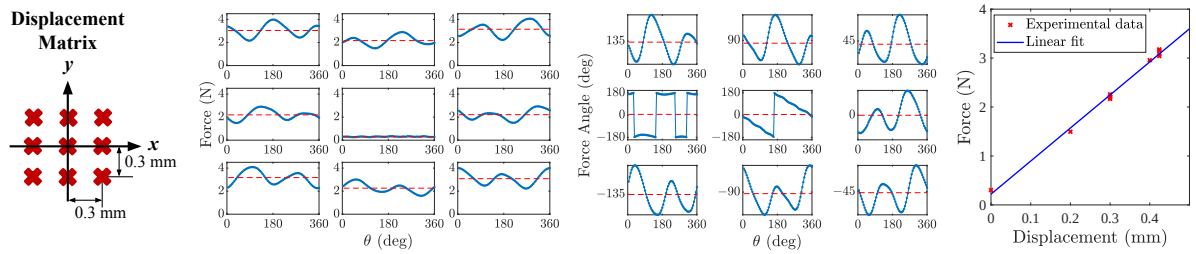

(a) (b) (c) (d)

Fig. 5: Displacement stiffness: (a) matrix, (b) force magnitude, (c) angle, and (d) k_δ curve fit

4.2. Torque constant

The torque constant k_t quantifies how much torque $\vec{T}$ an EM produces per torque current $\vec{i}_\mathrm{t}$ as shown in Table 2 Eq. (5). The winding configuration in Fig. 2 (a) is used to obtain torque due to its capability of torque-only generation with a single DC source. Fig. 6 (a) shows the torques measured under different current magnitudes, where the negative zero crossing angle of the curve is the location of the d-axis and is used as an offset angle for subsequent results. The peak torques satisfying the maximum torque-per-ampere condition are extracted to plot the linear fit as shown in Fig. 6 (b). The slope of the linear fit, k_t, is measured as 0.0164 Nm/A for this prototype.

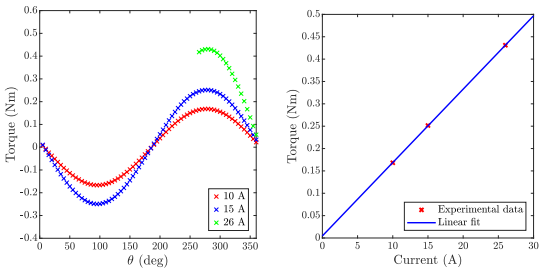

(a) (b)

Fig. 6: Torque versus (a) angle and (b) current

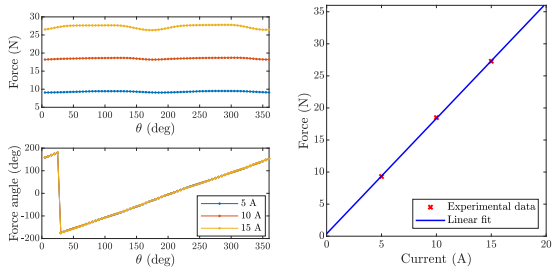

(a) (b)

Fig. 7: Force versus (a) angle and (b) current

4.3. Force constant

Force constant k_f defines the relationship between the suspension force $\vec{F}$ and the suspension current $\vec{i}_\mathrm{s}$ of the levitation system as shown in Table 2 Eq. (6). The winding configuration in Fig. 2 (b) is used since it enables force-only generation through a single DC current source. After measuring suspension forces with different currents as shown in Fig. 7 (a), a linear curve fit shown in Fig. 7 (b) should be generated using extracted peak force magnitudes to obtain the proportional slope, k_f. The force constant is found to be 1.797 N/A for this prototype.

4.4. Back electromotive force (back-EMF) constant

The back-EMF constant k_ϕ in Table 2 Eq. (7) characterizes the voltage $\vec{v}_\mathrm{m}$ induced in a coil per unit angular velocity ω. This is necessary for accurately decoupling back-EMF to achieve high-performance motor vector control and enable back-EMF-based sensorless control, as discussed in Upadhyaya et al. (2025).

For combined windings, the authors recommend testing in the parallel winding configuration of Fig. 8 (a) as this provides convenient diagnostic information: balanced back-EMF should be induced only at the motor inverter terminals and not the suspension terminals. Any voltage imbalance in the motor terminals likely indicates an unequal number of turns among the phases, whereas a non-zero voltage at the suspension-side suggests either rotor misalignment or an unequal number of phase turns–see Petersen and Severson (2025). Further, the resulting k_ϕ value should be validated against k_t from Section 4.2, as $k_\mathrm{t} \approx 3\sqrt{2}k_\phi$. Significant differences in this value indicate a problem in either the voltage or torque measurement that should be resolved before proceeding.

Figure 8 (b) presents the measured voltage when the rotor is operated at 5000 RPM. From the measured back-EMF, a linear fit of v_m shown in Fig. 8 (c) is obtained and k_ϕ is found as 3.79 mVrms/(rad/s) for this prototype.

4.5. T_m matrix

The T_m matrix is a generalized force-torque model that maps coil group currents to the force and torque they create, as described in Silber et al. (2005). It relates the electromagnetic force vector $\mathbf{F} = [F_x, F_y, \tau]^T$ to the coil

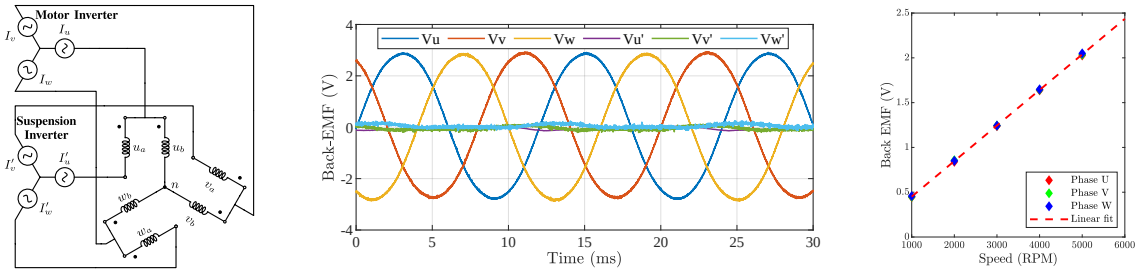

(a) (b) (c)

Fig. 8: (a) DPNV winding configuration, (b) Back-EMF measurements at 5000 RPM, and (c) k_ϕ curve fit

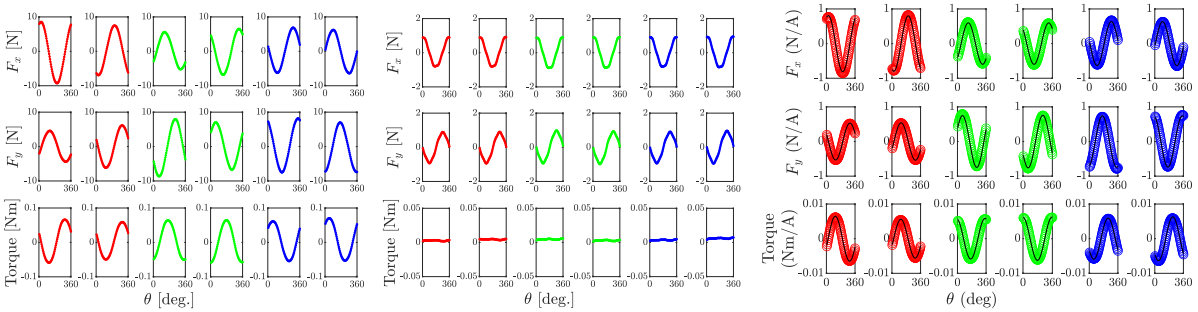

(a) (b) (c)

Fig. 9: T_m matrix: (a) raw data including cogging components, (b) cogging force and torque, and (c) T_m matrix

currents $\mathbf{i} = [i_1, i_2, i_3, i_4, i_5, i_6]^T$ as presented in Table 2 Eq. (8), where $T_\mathrm{m}(\theta)$ is a matrix representing the influence of each coil group on the force and torque, $M_\mathrm{c}(\theta)$ is a cogging force and torque vector. To determine the T_m matrix, DC currents should be injected into a single group while measuring force and torque over a full rotation. By subtracting the cogging components, Fig. 9 (b), from the raw data, Fig. 9 (a), the final T_m matrix is obtained through normalizing by current and fitting the results to sinusoidal functions as shown in Fig. 9 (c).

The T_m matrix is useful as a diagnostic tool and to calculate bearingless motor parameters. Engineers can confirm that each phase's characteristic is uniform and rotated appropriately from other phases. Discrepancies in this can indicate manufacturing issues, such as an inconsistent number of coil turns per phase, or measurement problems. Phase current vectors $\mathbf{i}$ can be calculated to excite force or torque over a rotor revolution and multiplied by the T_m matrix. The resulting force and torque can be compared against the earlier measured k_f and k_t to confirm that the machine is behaving linearly and to calculate torque ripple and force vector error. The T_m and M_c matrices can be used in Simulink to enable controls simulations to include full harmonic content, see Noguchi et al. (2025).

5. Sensor calibration methodology

This section introduces techniques to calibrate the sensors on the second test stand described in Section 3. Following these procedures ensures accurate feedback for stable levitation control. This section provides methodologies for shaft displacement and rotary position sensors as well as a procedure for finding the magnetic center.

5.1. Eddy current sensor calibration

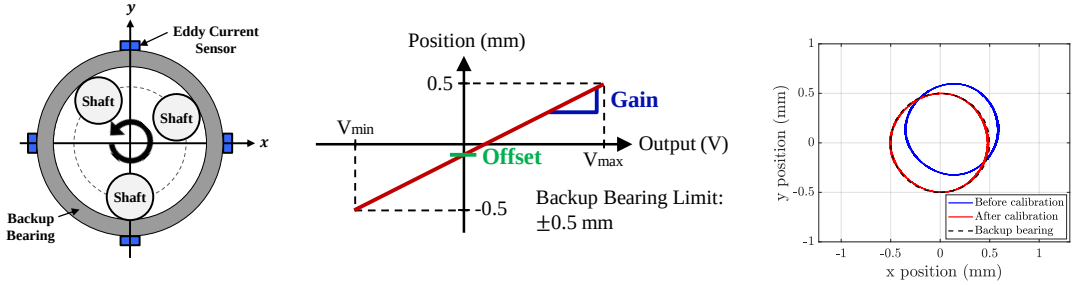

(a) (b) (c)

Fig. 10: Eddy current sensor: (a) calibration procedure, (b) linear map, and (c) calibration result

Accurate rotor displacement feedback requires precise conversion of sensor voltage to displacement mea-

surement. Even when factory calibration data is available, the sensor mounting tolerances and use of a curved target may mean that it cannot be accurately applied to the bearingless motor.

This procedure assumes that the bearingless motor is fitted with backup bearings that provide a known precision clearance for shaft displacement. Suspension currents are applied to shift the rotor along the backup bearing as illustrated in Fig. 10 (a). The sensor voltages are recorded to extract the gain and offset, see Fig. 10 (b). Figure 10 (c) shows the calibration result, where the calibrated output closely matches the backup bearing profile.

5.2. Encoder calibration

Accurate rotor position feedback is needed to separate d, q, x, and y axes in vector control. Position calibration is carried out in two sequential steps. The first step is without levitation: $\vec{i}_t = I_0 \angle 0°$ to generate a stator field that causes the d-axis of the rotor to align with the 0° electrical angle of the field direction. This alignment is used to determine the initial encoder offset and Fig. 11 (a) shows that the initial offset was determined as 813 encoder counts.

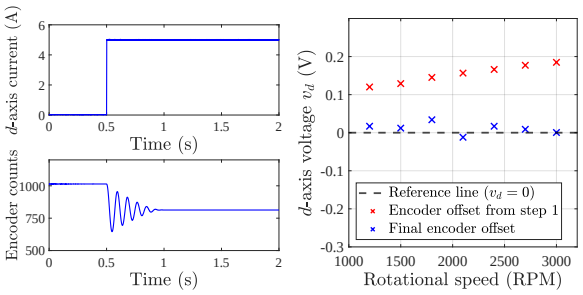

(a) (b)

Fig. 11: (a) Static and (b) rotational-encoder calibration

$$\begin{bmatrix} v_d \\ v_q \end{bmatrix} = \begin{bmatrix} R + pL & -\hat{\omega}_e L \\ \hat{\omega}_e L & R + pL \end{bmatrix} \begin{bmatrix} i_d \\ i_q \end{bmatrix} + \hat{\omega}_e \lambda_{\text{pm}} \begin{bmatrix} -\sin\tilde{\theta}_e \\ \cos\tilde{\theta}_e \end{bmatrix}, \quad \tilde{\theta}_e = \theta_e - \hat{\theta}_e \quad \text{(position error)} \tag{10}$$

The next step is to perform rotational encoder calibration while the rotor is levitated and spinning to account for dynamic factors that cannot be captured during the static calibration. Equations (10) from Upadhyaya et al. (2025) show that if the estimated angle offset is accurate, v_d becomes zero when both i_d and i_q are set to zero. The offset is determined as the value that minimizes v_d to nearly zero under no load torque (where $i_q \approx i_d = 0A$). After step 2, Fig. 11 (b) shows that a final encoder offset of 790 results in $v_d \approx 0$V across a range of speeds.

5.3. Find magnetic center

The magnetic center (MC) is the rotor displacement where suspension forces on the shaft match the expected load. In the example test stand, the x-axis suspension force is zero ($F_x = 0$) and the y-axis force should equal gravitational loading ($F_y = mg$). Identifying MC minimizes control effort and provides a reliable reference point for consistent control tuning.

The suspension forces are calculated using k_{f} measured in section 4.3 until finding the MC that yields balanced forces. Fig. 12 shows the forces measured at 3000 RPM at MC. The suspension forces in x-axis (F_{x1}, F_{x2}) for both machines are nearly zero, while the forces in y-axis (F_{y1}, F_{y2}) are nearly 2.3N, which corresponds to the weight of the prototype rotor.

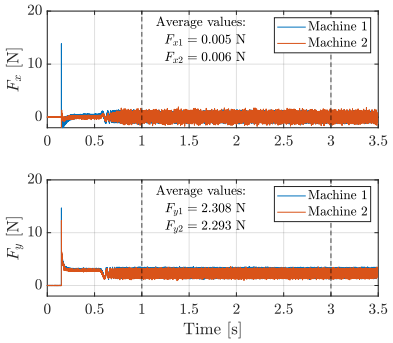

Fig. 12: Suspension forces at MC

6. System identification

Bearingless motor System ID procedures are now presented for the second test stand of Section 3. The tests require accurate machine parameters (Section 4) and sensor calibration (Section 5). The outcome is a measurement of the transfer functions in Table 1 as seen by the motor drive, which enables high performance controller tuning.

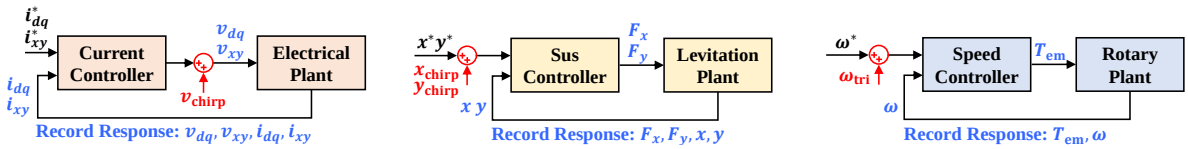

(a) (b) (c)

Fig. 13: Signal injection control block for (a) electrical, (b) levitation, and (c) rotary system

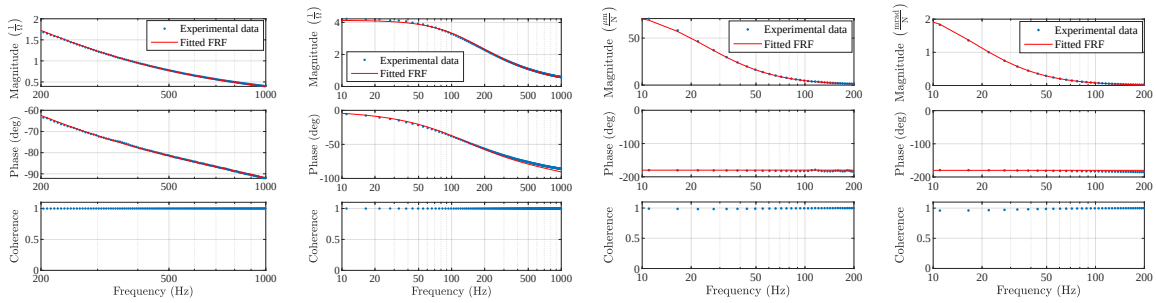

(a) (b) (c) (d)

Fig. 14: FRF results: (a) $\frac{I_x(s)}{V_x(s)}$ and (b) $\frac{I_d(s)}{V_d(s)}$ of electrical plant and (c) $\frac{y_0(s)}{F_{y_0}(s)}$ and (d) $\frac{\alpha(s)}{F_\alpha(s)}$ of levitation plant

6.1. Electrical plant system identification

The transfer function for electrical plant is given in Table 1 Eq. (1a) and (1b). To estimate the electrical plant parameters of R_{xy}, L_{xy}, R_{dq}, and L_{dq}, the control block for electrical plant System ID is shown in Fig. 13(a). This structure is based on the control system architecture in Fig. 1. To estimate the parameters, a voltage chirp signal across a frequency range is injected while the shaft is levitated and the response of currents is obtained to construct FRFs. As an example, the curve fitted FRFs of x and d axis are presented in Fig. 14 (a) and (b). The plot of the FRF demonstrates strong alignment between the experimental data and the fitted curve and high reliability of the measured data is implied since the coherence is unity across the entire frequency range.

6.2. Levitation plant system identification

As shown in Fig. 13 (b), x and y displacement chirp signals are injected to collect the displacement response for the levitation plant System ID. Then, the suspension force F_x, F_y is recorded to construct the FRF using the displacement response to identify the parameters k_δ and m in Table 1 Eq. (2a) and (2b). For centralized control depicted in Fig. 2, the same System ID methodology should be conducted for α and β-axis to determine J and k_δ in $\alpha\beta$ axis. As an example of the experimental results, the FRFs of y and α axes are shown in Fig. 14 (c) and (d). The experimental data for both y and α axes match well with the fitted curves of FRFs, which validates the identified k_δ and m parameters.

6.3. Rotary plant system identification

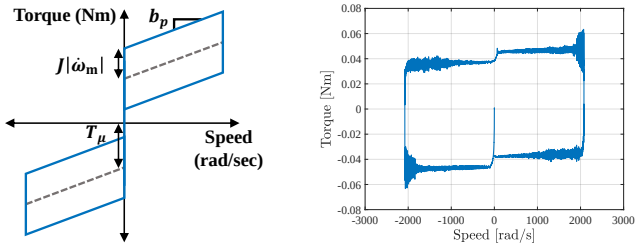

(a) (b)

Fig. 15: Flag plot of (a) ideal case, and (b) experimental result

Table 3: Rotary System ID results

Parameter	Estimate	Expected
J (kg·m^2)	29.54×10^{-6}	31.53×10^{-6}
b_p (kg·m^2/s)	4.28×10^{-6}	4.53×10^{-6}
T_μ (N)	0	0

To identify the parameters of the rotary plant system in Table 1 (3a) and (3b), a triangular speed (ω_{tri}) can be commanded as shown in Fig. 13 (c) to obtain the flag plot in Fig. 13 (a), see Johnson and Lorenz (1992). Its slope corresponds to damping b_p, width relates to inertia $J|\dot{\omega}_m|$, and vertical offset indicates friction torque T_μ. Sufficiently high peak speed ensures capturing the full span of the damping effects, and constant acceleration helps to obtain a decent estimation of inertia. A triangle-shaped speed command sweeping from –20 krpm to +20 krpm was applied to obtain Fig. 15. The flag plot shows symmetric slopes without an offset, indicating negligible friction torque. The estimated parameters listed in Table 3 confirm the accuracy of the modeling assumptions.

7. Conclusion

Poorly calibrated sensors and inaccurate plant parameters can all lead to unstable levitation when first com-

missioning a BM. Due to the high amount of interdependency in the control architecture, it is difficult to identify the root cause of failed levitation in new BMs. This paper addresses this problem by providing a structured approach to commission BMs that adapts proven techniques from EMs and MBs. The procedure is organized into three core phases as 1) system characterization, 2) sensor calibration, and 3) system identification that engineers can incorporate into their workflow when bringing up new BMs.

System characterization is introduced to determine the fundamental electromechanical parameters required for control design, including the displacement stiffness, torque constant, force constant, back-EMF constant, and the generalized force-torque T_{m} matrix. After determining static constants, calibration methodologies for displacement and angular position sensors are provided to ensure accurate feedback signals and a procedure is presented to find the MC where the net suspension forces on the rotor are balanced. Lastly, System ID methods are presented to determine the parameters of electrical, levitation, and rotary plants of BMs through control signal injection.

This paper presents comprehensive and practical guidelines for commissioning BMs by providing each procedure and its expected outcome, which will be a valuable reference for engineers developing their own BMs.

8. Acknowledgments and Conflicts of Interest

Research was sponsored by the U.S. Army Combat Capabilities Development Command (DEVCOM) Army Research Laboratory and was accomplished under Cooperative Agreement Number W911NF-20-2-0161. The views and conclusions contained in this document are those of the authors and should not be interpreted as representing the official policies, either expressed or implied, of the Army Research Laboratory or the U.S. Government.

References

Beya, K., Pintelon, R., Schoukens, J., Lataire, P., Guillaume, P., Mpanda-Mabwe, B., and Delhaye, M. (2002). Identification of synchronous machines parameters using broadband excitations. *IEEE Transactions on Energy Conversion*, 9(2):270–280.

Johnson, C. and Lorenz, R. (1992). Experimental identification of friction and its compensation in precise, position controlled mechanisms. *IEEE Transactions on Industry Applications*, 28(6):1392–1398.

Khamitov, A., Petersen, N. P., and Severson, E. L. (2023). Combined windings for bearingless motors—an overview. In *2023 IEEE Energy Conversion Congress and Exposition (ECCE)*, pages 4628–4635. IEEE.

Maslen, E. H., Schweitzer, G., Bleuler, H., and Cole, M. (2009). *Magnetic Bearings: Theory, Design, and Application to Rotating Machinery*. Springer.

Noguchi, T., Mokhtarabadi, M., Prasad, K., Gruber, W., and Severson, E. (2025). Model and control framework for bearingless motors with combined windings. In *19th International Symposium on Magnetic Bearings*, pages 1–8. ISMB.

Noshadi, A., Shi, J., Lee, W. S., Shi, P., and Kalam, A. (2015). System identification and robust control of multi-input multi-output active magnetic bearing systems. *IEEE Transactions on Control Systems Technology*, 24(4):1227–1239.

Petersen, N., Slininger, T., and Severson, E. L. (2022). State observers and run-out reduction for magnetically levitated motor systems. *IEEE Transactions on Industry Applications*, 59(2):1812–1823.

Petersen, N. P. and Severson, E. L. (2025). Rotor eccentricity impact on electromagnetic behavior in combined winding bearingless motors towards displacement self-sensing. *IEEE Transactions on Energy Conversion*, 40(1):323–336.

Silber, S., Amrhein, W., Bosch, P., Schob, R., and Barletta, N. (2005). Design aspects of bearingless slice motors. *IEEE/ASME Transactions on Mechatronics*, 10(6):611–617.

Upadhyaya, A., Nair, A. M., Petersen, N. P., and Severson, E. L. (2025). Back-EMF based self-sensing drive for ultra-high-speed surface mount PMSM. *IEEE Transactions on Industry Applications*. Early Access.